Chapter 4:

Synthesis and Characterization of Cobalt Doped Zinc Molybdenum Oxide (Co-$ZnMoO_4$) Nanostructure for Energy Applications

Amina Hassan, Hira Hafeez, Sami Ullah

DOI: 10.21467/books.186.4
Additional information is available at the end of the chapter

Due to the unstoppable depletion of natural fossil fuels and ongoing climate change, the world is currently developing new eco-friendly renewable energy sources that are abundant on the planet. Consequently, electrochemical energy storage devices are an effective approach to replacing fossil fuels. Here, for the first time, Cobalt-doped Zinc molybdenum oxide nanostructures (Co-$ZnMoO_4$ NSs) with 2%,4% and 6% concentrations were synthesized via a hydrothermal process and annealing treatment and were subsequently characterized using a variety of characterization methods to explore their electrochemical and physical properties. SEM micrographs showed particle like structure with random agglomeration morphology. The doping of Co into $ZnMoO_4$ was verified by the EDX results. Raman spectroscopy showed the new emerging peak of the nanostructure and gives information about the vibrational modes. Ultraviolet spectroscopy study indicated the band gap decreases as the concentration of Co increases. Additionally, for the first time, the electrochemical properties of Co-$ZnMoO_4$ NSs were investigated. For high-performance supercapacitors, the synthesized electrode material is a better choice to address continued demands for energy storage devices.

1. Introduction

Today, the two biggest problems mankind facing are environmental pollution and energy crisis. The scientific community is in search of an appropriate solution for these problems. Water is the most critical resource for terrestrial life and without water there would be no life [1]. One of the main issues is water quality. It has high sensitivity to release of toxic effluents from industries like textile industries which involve a number of complex processes like washing, bleaching, dyeing, printing and sizing into water ecosystem [2]. Fossil fuels, solar and nuclear energy are the primary energy sources. Solar energy is one of the most vital to life, as if the amount of solar radiation were to be reduced, all life would stop [3]. Less than one billionth of the sun's energy reaches the earth and less than 30% is absorbed by the land and ocean, the rest is reflected back into space [4]. Nevertheless, solar cells are a key element in transforming this energy into electrical energy, where they are used in today's buildings and even in satellites [5]. However, fossil fuels still provide approximately 80% of world energy supply, though fossil fuel and water are natural resources that are directly endangered by the accelerated industrialization. Oil and natural gas are still used extensively for transportation, cooking and heating. Due to their limited availability, new technologies have emerged over the last few years that aim to diminish their reliance on these technologies [6]. Air pollution, ozone

ISBN: 978-81-998984-9-3

depletion and severe health effects, such as being responsible for 2% of all cancer deaths [7] are caused by their combustion. An alternative and environmentally friendly solution is to use energy produced by the controlled fission of heavy atoms in a reactor to produce steam for driving turbines and producing electricity [8]. Renewable energy sources are sources that can be regenerated and that can help reduce the rate of climate change. These are hydroelectric, wind, geothermal and solar energy, and historically hydropower has accounted for over 50% of the global clean energy generation capacity [9]. While non-renewable energy resources are inexpensive and convenient to use, they are limited and pollute extensively and currently have an increasing competitive survival alternative of renewable energy sources that emit zero carbon [10]. Only approximately 10% of globally consumed energy comes from renewables while 90% comes from non-renewable sources [11]. This highlights the need for energy storage devices with electrochemical characteristics to enable this transition, which this chapter aims to solve by the use of metal oxide semiconductors. There are five categories of energy storage devices: electrochemical, thermal, electric, mechanical and chemical [12]. These include superior charge/discharge rate performance and cycle life compared to supercapacitors and electrochemical capacitors [13] and they are ideally suited for high power applications [14].

Supercapacitors (SCs) emerge as a groundbreaking energy storage solution. They are able to provide larger surface area electrodes and thin-dielectrics for higher capacitance than traditional capacitors and batteries [15]. This allows them to be used rather than batteries in automobiles and heavy industrial equipment, for which they have a high power density [16]. SCs are able to work in a limited window (2.5-2.7eV) and have several benefits including long cycle life, high specific capacitance, broad operating temperature range and environmental friendliness. These benefits derive from the redox reactions that are at the heart of their capacitive behavior, which are driven by electrode materials such as carbon nanotubes, graphene, conducting polymers, activated carbon, metal oxides and metal sulphides. They are also accompanied by liquid or gel electrolytes for high energy density and long cycle life [17], current collectors for high cell potential and durability [18], binders for maintaining the structure of the electrodes [19] and separators for ion transfer without contact between the electrodes. There are three types of SC. Electrostatic, non-Faradic charge storage techniques: electric double-layer capacitors (EDLCs) can provide high conductivity, high surface and excellent stability [20]. However, pseudocapacitors are able to store charge faradaically by the redox reactions at the electrode surface with the electrolyte whereas the EDLCs store less charge but have a longer life span [21, 22]. Hybrid capacitors use both mechanisms to get longer cycle life and stable voltage, but are more expensive and less energy dense than batteries [23]. The selection of electrode material is still the main factor in electrode performance, which should have high conductivity, thermal stability, chemical inertness, large surface area, corrosion resistance, and low price [21]. The advantages of overall SC characteristics are: fast charge/discharge, high energy and power density, long cycle and electrochemical stability, and flexibility in temperature and charge/discharge rate [24]. They are used for electric/hybrid cars, wind and photovoltaic power generation, electric power storage, elevators, pacemakers, cranes and UPS. The principal drawback is its low operating voltage which can be overcome by series connection of

ISBN: 978-81-998984-9-3

Book DOI: 10.21467/books.186

multiple SCs. Although high cost, low surface area, and toxicity are some drawbacks, transition metal oxides (TMOs) like NiO, Fe_2O_3, Co_2O_3, and V_2O_5 have become popular materials for pseudocapacitors because of their high power density, tunable oxidation state and potential for improving properties by doping [25, 26]. Doping introduces beneficial defects that enhance the conductivity, mobility of the carriers and the optical/electrical properties of the material [26]. Nanowires, nanotubes, and nanoflowers are examples of metal oxide nanostructures that are used in photocatalysis, energy harvesting, and quantum computing [27, 28]. In this regard, zinc molybdenum oxide, which can be reversibly charged, can be a semiconductor with high electrochemical capacity (952 mAh/g) and multiple oxidation state, and also has a large surface area, has been explored as a supercapacitor and lithium-ion battery material, but presents poor cycle stability [29, 30]. But the study of Co doped $ZnMoO_4$ (Co-$ZnMoO_4$) has not been done yet before. The motivation for this research is the gap between the low power density and specific capacitance of supercapacitors that can be addressed by using porous electrode materials with desirable charge/discharge properties. The ultimate goal is to provide a material with high specific capacitance and energy density that is both efficient and environmentally friendly and that could help alleviate the world energy crisis [31].

Various routes for the synthesis of $ZnMoO_4$ nanostructures with a controlled morphology and improved functional properties have been reported in the literature. Hydrothermal synthesis is the most popular method since it allows the precise control of particle size, crystal phase and morphology. Ramezani et al. synthesized rod-like nanostructures of $ZnMoO_4$ using various surfactant and solvents, and found that the morphology was affected by the use of polyethylene glycol and sodium dodecyl sulphate surfactants [32]. They showed that these nanostructures degraded 90% of the methyl orange after 6 hours under visible light after synthesis. In accordance with this, Pengxi Li et al. synthesized porous $ZnMoO_4$ nanosheets with oxygen vacancies and obtained high performance asymmetric supercapacitors by hydrothermal method and hydrogenation reduction method [33]. α-$ZnMoO_4$ nanoparticles were synthesized by Jie Fei et al., which were reported to be a possible anode material for lithium-ion batteries with high reversible capacity and strong cycling stability, under hydrothermal process [34]. D.M. Chernyak et al. optimized the growth of $ZnMoO_4$ crystals by doping with a small concentration of tungsten oxide without causing significant changes in the scintillation efficiency and the optical transmittance [35]. Bao-gai Zhai et al. prepared triclinic ZnMoO4 nanowires by air vapor deposition and achieved the single-crystalline nanowires with strong green PL [36]. Monoclinic $ZnMoO_4$ nanoparticles exhibited visible photoluminescence through hydrothermal synthesis with template agents reported by Runping Jia et al. [37] and flower-like rhombus-sheet morphologies with increasing reaction time reported by Gaoke Zhang et al. [38] using the same approach.

The structural, optical, and dielectric properties of $ZnMoO_4$ prepared by different methods such as solid-state, co-precipitation, precipitation, and sonochemical have been studied by several researchers. The synthesis of triclinic crystals of $ZnMoO_4$ using the solid state reaction method was reported by P. Yadav et al., who also reported a direct band gap of 4.12 eV with strong green photoluminescence, which makes

it suitable for phosphors, microwave devices, LEDs and transducers [39]. In a similar fashion, Sameer Kumar Tiwari et al. investigated the effect of Cu doping in α-$ZnMoO_4$, which resulted in a decrease in band gap from 3.6 to 2.78 eV and an improvement in the photoluminescence intensity with the improvement in the microwave dielectric properties *[40]*. Yu-Rou Jiang et al. synthesized β-$ZnMoO_4$ hydrothermally and found it to be an excellent visible-light photocatalyst for the degradation of phenol and Victoria Blue R [41]. $ZnMoO_4$ nanofibers were synthesized by Reza Roshani et al. by an ultrasonic bath process and excellent cycling stability was obtained along with high specific capacitance for use in supercapacitor applications [42]. Yanee Keereeta et al. used the electrospinning and calcination method to create the $ZnMoO_4$ nanofibers with an excellent optical property [43]. Li Lv et al. reported that complete degradation of methyl orange was achieved under UV irradiation with hydrothermally synthesized monoclinic $ZnMoO_4$ with blue-green photoluminescence [44]. H. Ait Ahsaine et al. prepared triclinic $ZnMoO_4$ by co-precipitation and observed the triclinic to monoclinic transition at 466 °C by thermal analysis [45]. Qingyun Ma et al. prepared cubic-like $ZnMoO_4$ by precipitation-freeze drying which exhibited better electrochemical performance and cycling stability than the conventional $ZnMoO_4$ [46].

The recent research has focused on the optimization of the morphology of $ZnMoO_4$ for electrochemical, photocatalytic, and optoelectronic properties. Y. Liang et al. have prepared nanorods and nanoplates of $ZnMoO_4$ by the ECLAL method and reported the improvement of optical properties of the resulting materials after annealing, suggesting their potential applications in photoelectric nanodevices [46]. ZnMoO4 nanorods synthesized using CTAB assisted hydrothermal method were found to be promising electrodes for supercapacitors due to its high specific capacitance of 779 Fg−1 and excellent cyclic stability over 3000 cycles as reported by Harichandran Gurusamy et al. [30]. B. Joji Reddy et al. synthesized α-$ZnMoO_4$ microspheres by a straightforward synthesis method and found that the specific capacitance of the material was 234.75 Fg^{-1} with 82% capacitance retention after 1600 charge–discharge cycles [47]. Under UV irradiation, high photocatalytic degradation efficiencies of the dye methylene blue and rhodamine B were achieved using a sonochemical method to synthesize nanoparticles of zinc molybdate ($ZnMoO_4$) by Indah Raya et al. Zahra Shahri et al. have designed a simple precipitation technique to produce uniform rod-like $ZnMoO_4$ nanostructures of high purity and desired morphology [48]. Last but not least, Jahangeer Ahmed et al. synthesized $ZnMoO_4$ submicron plates via hydrothermal method and found that they are greatly electrocatalytic for the hydrogen evolution reaction, which will have potential application for energy conversion [49].

2. MATERIALS AND METHODS

2.1 Material used

Chemicals and materials used for synthesis of ZnMoO4 and Co-ZnMoO4 NSs are Zinc nitrate hexahydrate [(Zn $(NO_3)_2.6H_2O$)], Sodium molybdate dehydrate [$Na_2MoO_4.2H_2O$], Ammonium fluoride [(NH_4F)], Cobalt nitrate hexahydrate [$Co(NO_3)_2.6H_2O$], Distilled water (H_2O), and Ethanol (C_2H_5OH). All solutions

were prepared in deionized water, and ethanol was used for washing prepared solid samples. 2M KOH Alkaline solution was employed as an electrolyte for electrochemical analysis.

2.2 Synthesis Process

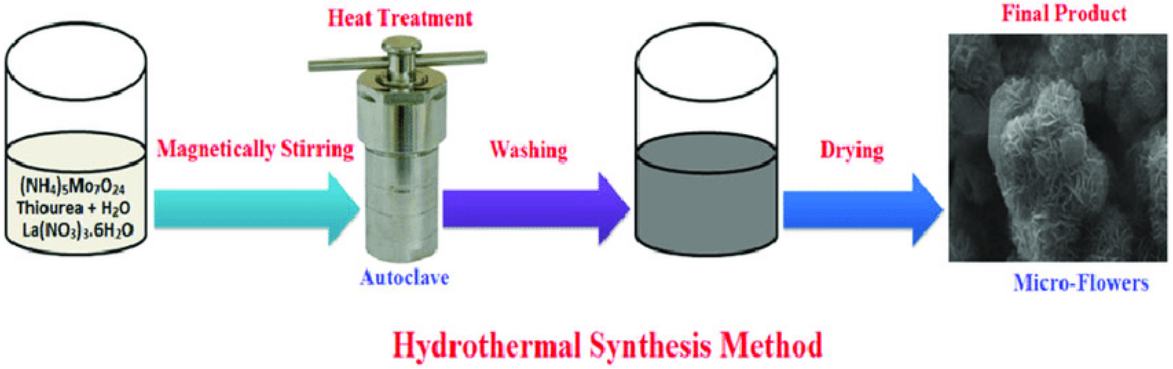

Figure 4.1: Working diagram of $ZnMoO_4$ NSs.

There are several methods available for the synthesis of pure zinc molybdate ($ZnMoO_4$) and cobalt-doped zinc molybdate (Co–$ZnMoO_4$) nanostructures, including sol-gel, co-precipitation, solid-state reaction, and hydrothermal techniques. Among these, the hydrothermal method was selected in the present study because it is a simple, cost-effective, and environmentally friendly approach that produces highly crystalline nanostructures with high yield, controlled morphology, and excellent purity under relatively mild reaction conditions.

The hydrothermal method was employed for the synthesis of pure $ZnMoO_4$ nanostructures, and the schematic representation of the synthesis procedure is shown in **Figure 4.1**. Initially, the required quantities of the precursor materials were accurately weighed using a digital analytical balance. Specifically, 0.29749 g of zinc nitrate hexahydrate [$Zn(NO_3)_2{\cdot}6H_2O$], 1.23586 g of sodium molybdate dehydrate ($Na_2MoO_4{\cdot}2H_2O$), and 0.0741 g of ammonium fluoride (NH_4F) were dissolved in a mixed solvent containing 25 mL of deionized water and 5 mL of ethanol. The resulting solution was continuously stirred on a magnetic stirrer for 30 minutes to obtain a homogeneous reaction mixture.

After complete mixing, the prepared solution was transferred into a 50 mL Teflon-lined stainless-steel autoclave, which was tightly sealed and placed in a temperature-controlled oven. The hydrothermal reaction was carried out at 160°C for 12 hours. Upon completion of the reaction, the autoclave was allowed to cool naturally to room temperature before opening. The obtained precipitate was then collected by filtration and thoroughly washed three times with distilled water and once with ethanol to remove any unreacted precursors and impurities. The washed product was transferred to a china dish and dried in an oven at 60°C for 4 hours. After drying, pure $ZnMoO_4$ powder was obtained and preserved for further characterization. In addition to the undoped $ZnMoO_4$ sample, four cobalt-doped $ZnMoO_4$ samples were synthesized by

introducing cobalt at different concentrations, including **2 wt.%**, while keeping the remaining synthesis conditions unchanged, as illustrated in **Figure 4.1**.

2.3 Material Characterizations

The structural, morphological, optical, and electrochemical properties of the synthesized electrode material were systematically investigated using various diagnostic instruments. Crystallographic phases were evaluated via X-ray diffraction (XRD, Tongda TD-3700) using $Cu - K_\alpha$ radiation ($\lambda = 1.5406\dot{A}$ across a 2θ range of $20^o - 60^o$. Dopant incorporation was verified using a GMD PROTRUSTECH Raman spectrometer, while surface morphology was examined using a scanning electron microscope (SEM, MAIA3 TESCAN). Optical absorption characteristics were recorded in the 350–900 nm spectral range with a C7200 UV-Vis spectrophotometer. Finally, the electrochemical performance of the electrode material was measured using a GAMRY Potentiostat Interface 5000 (Model 14543).

3. Results and Discussion

3.1 Scanning Electron Microscopy (SEM)

SEM analysis revealed the morphology of synthesized undoped $ZnMoO_4$ and Co-$ZnMoO_4$ NSs with 2% and 6% concentration as observe in **Figure 4.2. Figure 4.2(a_1-a_3)** exhibited the particle-like structure with random agglomeration of undoped $ZnMoO_4$ NSs at different magnification. **Figure 4.2(**b_1-b_3**)** shows the micrographs of the as-synthesized 2% Co-$ZnMoO_4$ NSs. It is clearly observed that the morphology of prepared material changed due to co doping. **Figure 4.2(c_1-c_3)** of prepared sample (6 % Co-$ZnMoO_4$ NSs) at different magnification depict that the size of particles decreases by increasing dopant (Co) concentration and morphology changed with spherical particle and uniformly distributed.

3.2 X-ray Diffraction Analysis (XRD)

The crystallographic structure of the as-prepared material was analyzed by an X-ray diffractometer. XRD diffractograms of $ZnMoO_4$ NSs and 2% and 4% Co-doped $ZnMoO_4$ NSs are shown in **Figure 4.3 (a- b).** All well-defined peaks associated with planes (110), (020), (002), (112), (220) and (131) correspond to the $2\theta_{25.71°}$, $2\theta_{31.8°}$, $2\theta_{36.6°}$, $2\theta_{44.1°}$, and $2\theta_{50.7°}$ and $2\theta_{54.9°}$ respectively. These distinct peaks are assigned to the monoclinic phase and are in accord with the "JCPDS card No. 25–1024" of $ZnMoO_4$. The characteristics peak (110) at $2\theta=25.71^0$ is the strong agreement of $ZnMoO_4$ NSs. The extremely crystalline nature of the prepared NSs is shown by sharp peaks.

Debye Scherrer formula was used to determine the average crystallite size (D) of the prepared materials **(eq 4.1)** [49].

$$D = K\lambda / \beta Cos\theta \qquad (4.1)$$

Where λ is the wavelength of Cu Kα radiation (λ = 1.5406 Å), β is the full-width at half maximum, θ is the diffraction angle, and K is the shape factor (0.88). The average grain size of $ZnMoO_4$ NSs was reduced by

increasing Co concentration. The computed crystallite sizes were 26.63 , 20.37, and 18.10 nm for undoped $ZnMoO_4$ NSs, 2% Co- $ZnMoO_4$ NSs and 6% Co- $ZnMoO_4$ NSs respectively

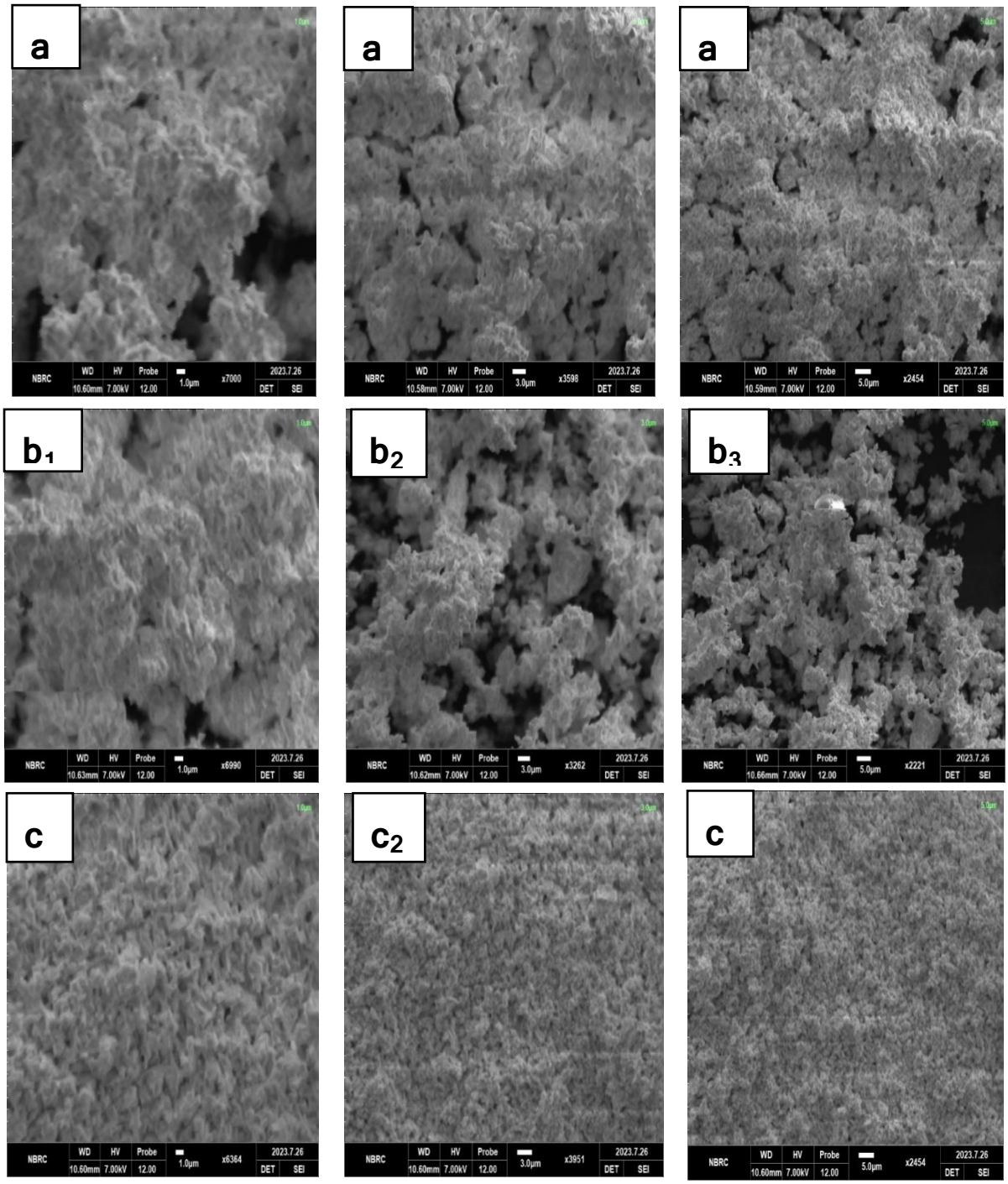

Figure 4.2: SEM micrographs (a_1-a_3) undoped $ZnMoO_4$ NSs, (b_1-b_3) 2% Co- $ZnMoO_4$ NSs and (c_1-c_3) 6% Co-$ZnMoO_4$ NSs at various magnifications.

3.3 Fourier Transform Infrared Spectroscopy (FTIR)

An efficient analytical technique for examining how molecules interact with infrared light is FTIR spectroscopy. It involves measuring the absorption of infrared light by a sample and generating a spectrum that represents this absorption as a function of frequency. FTIR spectroscopy was utilized to

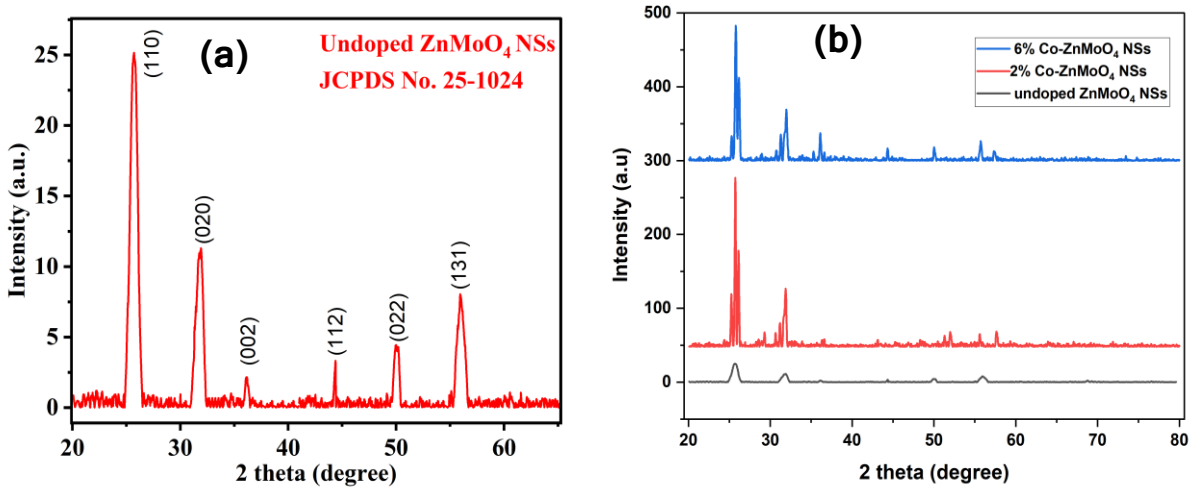

Figure 4.3: XRD pattern of a) Undoped $ZnMoO_4$ NSs b) Undoped $ZnMoO_4$, 2% and 6% Co-$ZnMoO_4$ NSs.

analyze chemical bonds and identify functional groups present in as-prepared $ZnMoO_4$ and 2%, 4%, 6%, Co doped $ZnMoO_4$. In the case of the provided figures, **Figure 4.4 (a)** represents the spectrum of pure MoO_4 nanosheets (NSs), while **Figure 4.4 (b**) displays the spectra of pure MoO_4 NSs, $ZnMoO_4$ NSs, 2% Co-$ZnMoO_4$ NSs, 4% Co-$ZnMoO_4$ NSs, and 6% Co-$ZnMoO_4$ NSs. The frequency range between 700 and 980 cm^{-1} corresponds to specific vibration modes associated with distorted $(MoO_4)^{2-}$ tetrahedrons, as reported in previous studies [50-52].

These vibrational modes provide valuable information about the structure and behavior of the $(MoO4)^{2-}$ tetrahedrons within the analyzed samples. The attribution of these modes has been documented in the literature, indicating that researchers have previously identified and characterized these specific vibrational features. Additionally, the bands at 1633 cm^{-1} and 3435 cm^{-1} in the spectra that were observed correspond to vibrations of the molecules H-O-H bending and stretching, respectively. These vibrational motions involve the bending of hydrogen-oxygen-hydrogen bonds and the stretching of oxygen-hydrogen bonds within the molecules or ions under investigation. By analyzing the FTIR spectra and identifying these vibrational modes and bands, researchers gain insights into the composition, structural features, and molecular behavior of the samples. This information is valuable for understanding the characteristics and potential uses of the materials under study, as well as for future study and development in related fields. Such structural changes are known to create more oxygen vacancies and defect sites, increasing electrical conductivity and the number of electrochemically active centers. Furthermore, the presence of surface hydroxyl groups enhances electrolyte wettability, allowing for effective ion transport during charge-discharge operations. These combined effects improve the capacitance, charge-transfer kinetics, and cycling stability of the doped oxide electrode.

ISBN: 978-81-998984-9-3

Book DOI: 10.21467/books.186

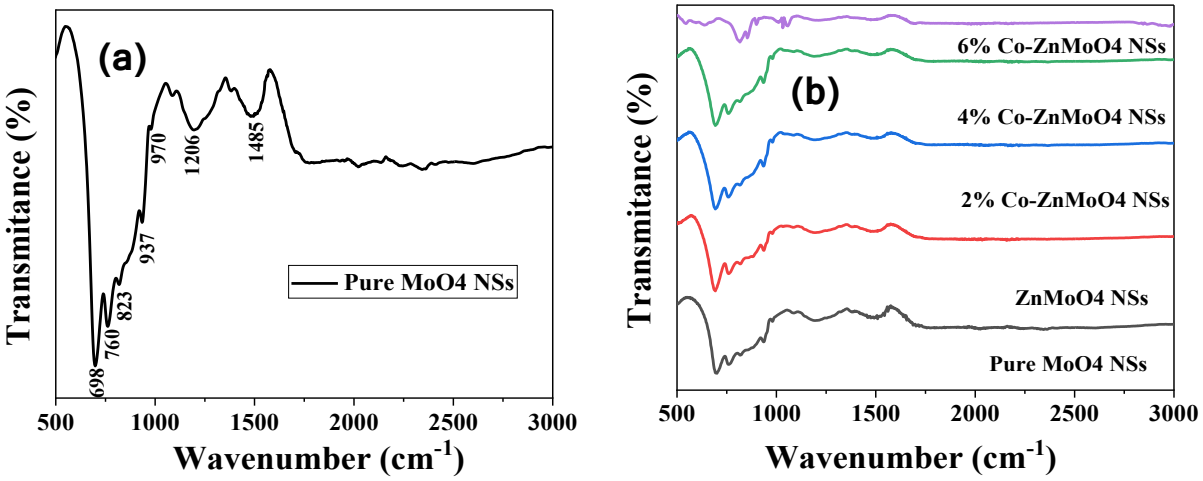

Figure 4.4: FTIR spectra of a) Undoped $ZnMoO_4$ NSs and (b) Undoped $ZnMoO_4$ and 2%, 4%, and 6% Co- $ZnMoO_4$ NSs.

3.4 Raman Spectroscopy

Figure 4.5 (a -b) presents the Raman spectra of synthesized samples of undoped $ZnMoO_4$ NSs**, 2%** and 6% Co-$ZnMoO_4$ NSs. The spectrum exhibits normal Raman scattering bands characteristic of MoO_4 crystalline phase. MoO_4 vibration is responsible for the strong band at 321 cm^{-1}, which indicates that the synthesized sample contains Mo-O bonds as shown in **Figure 4.5 (a)**. The doubly coordinated oxygen (Mo_2-O_2) extending mode, which accounts for the peak at about 821 cm^{-1}, results from two octahedral molecules sharing a corner of oxygen [53, 54]. This peak is a signature of MoO_4 and confirms the existence of crystalline phase. Molybdenum oxide is present in the sample as indicated by the peak at 880 cm^{-1}, which is attributed to the Mo=O bond. Finally, the peak at approximately 905 cm^{-1}, which results from an unshared oxygen in Mo, is caused by the $ZnMoO_4$ mode. The peak positions agree well with the literature values for the α -MoO_4 crystalline phase, indicating that the synthesized sample is of high purity [55, 56]. By increasing Co doping, the peak shifted slightly towards higher wave number that confirmed the incorporation of Co-doped in $ZnMoO_4$ as exhibit in **Figure 4.5(b).** The Raman spectroscopy analysis provides valuable evidence about the chemical and structural characteristics, of the synthesized sample, which is crucial for comprehending the synthetic sample's potential applications in numerous fields, including photocatalysis and energy storage devices and photocatalysis.

3.5 Ultraviolet Visible Spectroscopy of $ZnMoO_4$ nanostructures

Ultraviolet Visible spectroscopy technique used to analyze how molecules interact with ultraviolet (UV) and visible light. When monochromatic light strikes the synthetic material, atomic electrons absorb it and continue to do so until they enter their excited states, which results in an adsorption peak. This fascination reduces the intensity of transmitted or reflected light. By measuring this light, a spectrophotometer provides information about a substance's electronic structure, composition, and concentration. The resulting

absorption spectrum displays peaks at wavelengths of absorbed light, aiding in characterization and analysis. UV-visible spectroscopy of as prepared. $ZnMoO_4$ and 2%, 4% and 6%

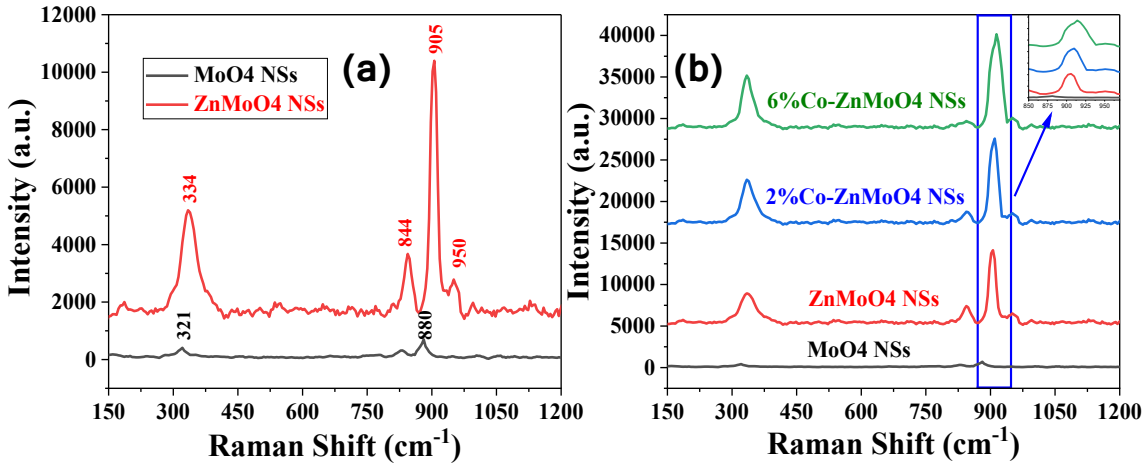

Figure 4.5: Raman Spectra of synthesized a) Undoped $ZnMoO_4$ NNs (b) Undoped $ZnMoO_4$ NSs and 2%, 4% and 6% Co- $ZnMoO_4$ NSs.

CO-doped $ZnMoO_4$ NSs were done at room temperature with ethanol as a solvent. Each solution was prepared by adding the same ratio of sample to 10ml of ethanol. The **Figure 4.6 (a)** exhibit pure MoO_4 absorption spectra, the UV-visible spectrum show absorption peaks related to the electronic transitions in the MoO_4 ion at 425 nm. Pure MoO_4 ions typically absorb in the visible region, with peaks in the range of 200-500 nm. Various elements, including pH and the presence of other ions, can affect the precise location and intensity of the peaks. The **Figure 4.6 (b)** shows $ZnMoO_4$, 2%, 4%, and 6% Co-$ZnMoO_4$ NSs that contains both Zn^{2+} and MoO_4 2- ions. Due to electronic transitions in both the MoO_4^{2-} and Zn^{2+} ions, ZnMoO4 exhibits absorption peaks in the UV-visible spectrum. The specific electronic configurations and the coordination environment surrounding each ion determine the locations and intensities of these peaks. The samples with 2%, 4%, and 6% Co-$ZnMoO_4$ refer to Co-doped $ZnMoO_4$ samples. The presence of cobalt ions introduce additional electronic transitions and may modify the absorption characteristics compared to pure MoO_4 and absorption peak slightly shift towards higher wavelength indicted the in incorporation of co doping. Depending on the cobalt ion concentration and how they interact with the MoO_4 matrix, different absorption peaks and their intensities are observed. The spectra obtained would provide specific information about the absorption characteristics of each sample in terms of peak positions, intensities, and shapes, allowing for a more comprehensive analysis of their electronic structure. Utilizing the Tauc relation or Tauc plot, the energy band gap of the prepared sample was determined.

$$(\alpha h\upsilon)^n = C(h\upsilon - Eg) \qquad (4.2)$$

Where hυ is the photon energy, Eg is the energy band gap, C is the constant value, and the value of n= 2, 1/2, 3/2 denoted the different energy band gap such as direct, indirect, and forbidden similarly. This

relation is utilized to calculate the energy bandgap of Pure MoO_4, $ZnMoO_4$, 2%, 4%, and 6%Co doped $ZnMoO_4$ NSs.

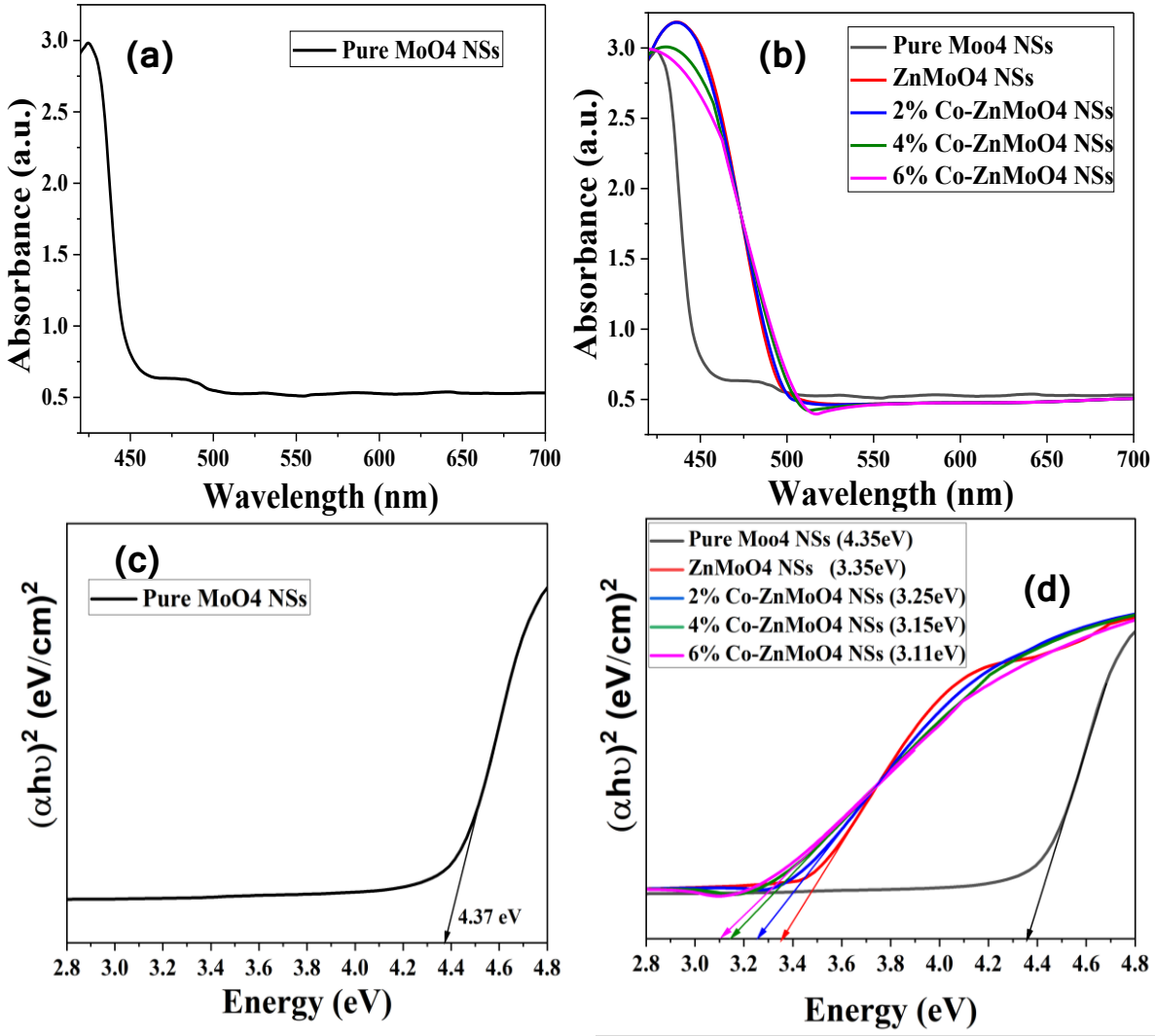

Figure 4.6: UV-Visible spectra of **(a)** $ZnMoO_4$ NSs, **(b)** $ZnMoO_4$ 2%, 4%, and 6% Co-doped $ZnMoO_4$ NSs, **(c)** Direct band gap energy of $ZnMoO_4$ 2%, 4%, and 6% Co-doped $ZnMoO_4$NSs.

The calculated optical direct energy band gap of $ZnMoO_4$ and 2%, 4%, 6% Co-doped $ZnMoO_4$ NSs were 3.35eV, 3.25eV, 3.15eV, 3.11eV respectively. The observed direct energy band gaps of as-prepared NSs decreased with increasing the concentration of Co from 3.35eV to 3.11eV as shown in **Figure 4.6(c-d)** and presented in **Table 4.1.**

Table 4.1. Reported $ZnMoO_4$ NSs energy bandgap.

Material	Direct bandgap (eV)	Reference
$ZnMoO_4$ NSs	3.29	[36]
$ZnMoO_4$ NSs	3.35	This work

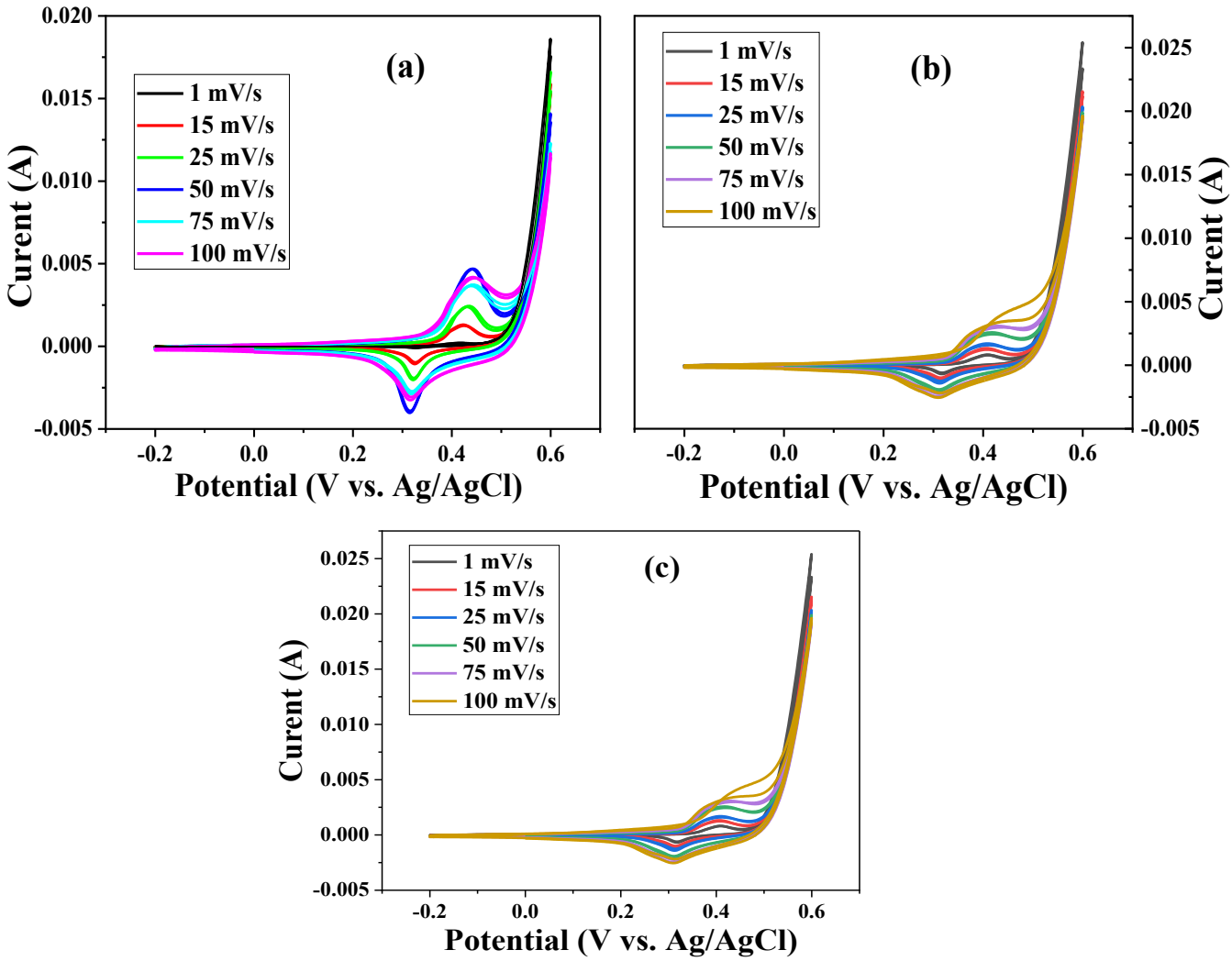

Figure 4.7: Cyclic Voltammogram of $ZnMoO_4$ (a-c) and 2%, 6% Co- $ZnMoO_4$ NSs.

3.6 Cyclic Voltammetry (CV)

In three-electrode systems, cyclic voltammetry is an eminent electrochemical characterization technique behind the charge storage mechanism. CV measurements of $ZnMoO_4$, 2% Co- $ZnMoO_4$, and 6% Co-$ZnMoO_4$ NCs as shown in the **Figure 4.7(a-c)** were carried out at different scan speeds of $1mVs^{-1}$, 10 mVs^{-1}, 15 mVs^{-1}, $25mVs^{-1}$, $75mVs^{-1}$ and $100mVs^{-1}$ with an operating potential window (PW) -0.2 to 0.6 eV by using 2M KOH solution. The CV analysis expresses the noticeable redox peak at the particular potential

that indicates the enrich redox nature of the prepared material. During the charging and discharging mechanism, faradic reactions of the of the electrode material are indicated by cluster of redox peaks. The reaction mechanism is significantly influenced by the potential scan speed. The area under the CV curves represents the overall charge that has been stored in the electrodes. As the potential scan speed decreases from 75 mVs^{-1} to 5 mVs^{-1} by shifting the anodic peak to a negative potential and the cathodic peak to a positive potential, it appears that the redox current is decreases. On the other hand the area of curve increases by increasing the san rate, indicating that the electrode has improved charge storage and good reversibility. The well-defined peaks at all conceivable scan rates, which may be explained by a capacitive charge storage mechanism, demonstrate the existence of the faradic charge transfer. The charge storage capacity was seen in the region under the curve.

The Cp of the fabricated electrodes was attained by equation.

$$C_p = A/2KmΔV \qquad (4.3)$$

Where, ΔV (V_2 - V_1) is the potential window, m is the mass of active material, K is the scan rate, A is the absolute surface area. The computed values of Cp for all the designed electrodes are presented in **Table 4.2.** Remarkably, the maximum Cp value obtained from CV curve at scan rate of mVs^{-1} EIS of $ZnMoO_4$ and Co- $ZnMoO_4$ NSs.

Table 4.2: The C_p values for all the designed electrodes

Materials	50 mV/s F/g	25 mV/s F/g	15 mV/s F/g	5 mV/s F/g	1 mV/s F/g
Undoped $ZnMoO_4$	81	135	167	286	1022
2% Co-$ZnMoO_4$	134	192	232	464	1281
6% Co-$ZnMoO_4$	180	282	469	606	**1535**

3.7 Electrochemical Impedance Spectroscopy (EIS)

The electrochemical behavior (current conductivity and internal resistance) of the as-synthesized material is characterized using the EIS technique. EIS analysis was evaluated at open circuits between the frequencies of 100 KHz and 0.1 Hz. The low, medium, and high regions frequently exhibit impedance character. Supercapacitors frequently have electrochemical characteristics halfway between those of capacitors and resistors. At low frequency the electrochemical system act as capacitor and at high frequency like a resistance. At high frequencies, the electrochemical capacitor behaves like a resistor, while at low frequencies, it behaves like a capacitor, as shown in **Figure 4.8(a, b).**

Compared to the $ZnMoO_4$ and 2% Co-$ZnMoO_4$ samples, the diameter semicircle of the 6% Co-$ZnMoO_4$ sample is considerably smaller. Due to the increased conductivity, this smaller semicircle suggests lower charge transfer resistance. Low charge transfer resistance and high conductivity are characteristics of the

smaller semicircle. The diffusion of ions between the electrolyte and electrode surface is responsible for the vertical line, which also demonstrates that electrode material is approaching to nearly an ideal capacitor [58].

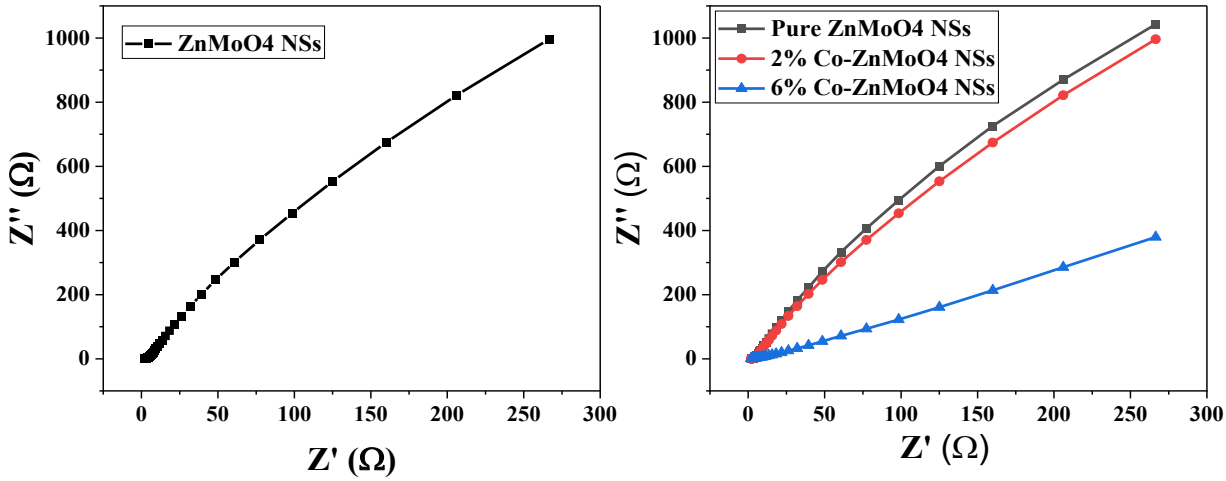

Figure 4.8: EIS spectra of $ZnMoO_4$ and 2%, 6% Co-$ZnMoO_4$ NSs.

4. Conclusion

In summary, for the first time Zinc molybdenum oxide ($ZnMoO_4$ NSs) and Cobalt-doped Zinc Molybdenum oxide nanostructures (Co-$ZnMoO_4$NSs) with 2%, 4% and 6% were synthesized via affordable hydrothermal method. The formation of nanoparticles was confirmed by SEM micrographs. SEM micrographs showed randomly particle like morphology. EDX spectra confirmed the successful doping in $ZnMoO_4$ NSs. The crystalline size of $ZnMoO_4$ NSs were examined by XRD. The Raman spectroscopy gave the information about the vibrational modes. The absorption spectra and energy band gap of prepared samples were calculated by Tauc relation in Ultra- Violet visible Spectroscopy. Uv-Vis analysis showed the band gap decreases as the concentration of Co increases. In Cyclic Voltammetry the specific capacitance of ZnMoO4 NSs, 2% and 6% Co-$ZnMoO_4$ NSs was to be calculated. Based on the findings, Co-$ZnMoO_4$ nanostructures is useful electrode material for electrochemical supercapacitor applications.

5. Publisher's Note

AIJR remains neutral with regard to jurisdictional claims in published maps and institutional affiliations.

Author's Detail

Amina Hassan, Hira Hafeez, Sami Ullah*
Department of Physics, University of Okara, Okara, Pakistan.

*Corresponding author

How to Cite this Chapter:

A. Hassan, H. Hafeez, S. Ullah, "Synthesis and Characterization of Cobalt Doped Zinc Molybdenum Oxide (Co-$ZnMoO_4$) Nanostructure for Energy Applications," in *Emerging Functional Materials for a Sustainable Energy Future*, M. A. Kamran, Ed. India: AIJR Publisher, 2026, pp. 59-74. ISBN: 978-81-998984-9-3, doi: 10.21467/books.186.4

References

[1] F. Chien, H. W. Kamran, G. Albashar, and W. J. I. J. o. H. E. Iqbal, "Dynamic planning, conversion, and management strategy of different renewable energy sources: a sustainable solution for severe energy crises in emerging economies," vol. 46, no. 11, pp. 7745-7758, 2021.

[2] B. P. J. E. S. P. Chaplin and Impacts, "Critical review of electrochemical advanced oxidation processes for water treatment applications," vol. 16, no. 6, pp. 1182-1203, 2014.

[3] P. E. J. S. Glaser, "Power from the sun: Its future," vol. 162, no. 3856, pp. 857-861, 1968.

[4] F. Al-Enezi, J. Sykulski, and N. A. J. E. P. Ahmed, "Visibility and potential of solar energy on horizontal surface at Kuwait area," vol. 12, pp. 862-872, 2011.

[5] R. C. Neville, *Solar energy conversion: the solar cell*. Elsevier, 1995.

[6] P. Seljom and E. J. I. J. o. E. S. M. Rosenberg, "A study of oil and natural gas resources and production," vol. 5, no. 1, pp. 101-124, 2011.

[7] F. Barbir, T. Veziroğlu, and H. J. I. j. o. h. e. Plass Jr, "Environmental damage due to fossil fuels use," vol. 15, no. 10, pp. 739-749, 1990.

[8] C. D. Ferguson, *Nuclear energy: What everyone needs to know*. OUP USA, 2011.

[9] A. Ignatyuk, O. Liubkina, T. Murovana, and A. Magomedova, "FinTech as an innovation challenge: From big data to sustainable development," in *E3S Web of Conferences*, 2020, vol. 166, p. 13027: EDP Sciences.

[10] R. A. Salim, K. Hassan, and S. J. E. e. Shafiei, "Renewable and non-renewable energy consumption and economic activities: Further evidence from OECD countries," vol. 44, pp. 350-360, 2014.

[11] R. M. J. E. J. o. s. D. r. Elavarasan, "The motivation for renewable energy and its comparison with other energy sources: A review," vol. 3, no. 1, p. em0076, 2019.

[12] A. A. Kebede, T. Kalogiannis, J. Van Mierlo, M. J. R. Berecibar, and S. E. Reviews, "A comprehensive review of stationary energy storage devices for large scale renewable energy sources grid integration," vol. 159, p. 112213, 2022.

[13] A. Slesinski, K. Fic, and E. Frackowiak, "New trends in electrochemical capacitors," in *Advances in Inorganic Chemistry*, vol. 72: Elsevier, 2018, pp. 247-286.

[14] M. E. Amiryar and K. R. J. A. S. Pullen, "A review of flywheel energy storage system technologies and their applications," vol. 7, no. 3, p. 286, 2017.

[15] A. Afif, S. M. Rahman, A. T. Azad, J. Zaini, M. A. Islan, and A. K. J. J. o. E. S. Azad, "Advanced materials and technologies for hybrid supercapacitors for energy storage–A review," vol. 25, p. 100852, 2019.

[16] A. Burke, Z. Liu, and H. Zhao, "Present and future applications of supercapacitors in electric and hybrid vehicles," in *2014 IEEE International Electric Vehicle Conference (IEVC)*, 2014, pp. 1-8: IEEE.

[17] C. Zhong, Y. Deng, W. Hu, J. Qiao, L. Zhang, and J. J. C. S. R. Zhang, "A review of electrolyte materials and compositions for electrochemical supercapacitors," vol. 44, no. 21, pp. 7484-7539, 2015.

[18] A. K. Samantara and S. Ratha, "Materials development for Active/Passive components of a supercapacitor: background, present status and future perspective," 2017.

[19] K. Tõnurist, T. Thomberg, A. Jänes, I. Kink, and E. J. E. C. Lust, "Specific performance of electrical double layer capacitors based on different separator materials in room temperature ionic liquid," vol. 22, pp. 77-80, 2012.

[20] J. Liu *et al.*, "Advanced energy storage devices: basic principles, analytical methods, and rational materials design," *Advanced science,* vol. 5, no. 1, p. 1700322, 2018.

[21] K. V. G. Raghavendra *et al.*, "An intuitive review of supercapacitors with recent progress and novel device applications," vol. 31, p. 101652, 2020.

[22] K. Sharma, A. Arora, and S. K. J. J. o. E. S. Tripathi, "Review of supercapacitors: Materials and devices," vol. 21, pp. 801-825, 2019.

[23] M. S. Halper and J. C. J. T. M. C. Ellenbogen, McLean, Virginia, USA, "Supercapacitors: A brief overview," vol. 1, 2006.

[24] P. Lannelongue *et al.*, "“Water-in-Salt” for supercapacitors: a compromise between voltage, power density, energy density and stability," vol. 165, no. 3, p. A657, 2018.

[25] G. K. Veerasubramani, K. Krishnamoorthy, S. Radhakrishnan, N.-J. Kim, and S. J. J. I. j. o. h. e. Kim, "Synthesis, characterization, and electrochemical properties of CoMoO4 nanostructures," vol. 39, no. 10, pp. 5186-5193, 2014.

[26] F. Sanakousar, C. Vidyasagar, V. Jiménez-Pérez, and K. J. M. s. i. s. p. Prakash, "Recent progress on visible-light-driven metal and non-metal doped ZnO nanostructures for photocatalytic degradation of organic pollutants," vol. 140, p. 106390, 2022.

[27] S. Nie, Y. Xing, G. J. Kim, and J. W. J. A. R. B. E. Simons, "Nanotechnology applications in cancer," vol. 9, pp. 257-288, 2007.

[28] J. Contreras, E. Rodriguez, and J. J. E. P. S. R. Taha-Tijerina, "Nanotechnology applications for electrical transformers—A review," vol. 143, pp. 573-584, 2017.

[29] A. Awan *et al.*, "Green synthesis of molybdenum-based nanoparticles and their applications in energy conversion and storage: a review," vol. 47, no. 72, pp. 31014-31057, 2022.

[30] H. Gurusamy, R. Sivasubramanian, Y. Johnbosco, and M. J. C. P. Bhagavathiachari, "Morphology-controlled synthesis of one-dimensional zinc molybdate nanorods for high-performance pseudocapacitor electrode application," vol. 75, pp. 1715-1726, 2021.

[31] Y. Liu, Q. Wu, L. Liu, P. Manasa, L. Kang, and F. J. J. o. m. c. A. Ran, "Vanadium nitride for aqueous supercapacitors: a topic review," vol. 8, no. 17, pp. 8218-8233, 2020.

[32] M. Ramezani, S. M. Hosseinpour-Mashkani, A. Sobhani-Nasab, and H. J. J. o. M. S. M. i. E. Ghasemi Estarki, "Synthesis, characterization, and morphological control of ZnMoO 4 nanostructures through precipitation method and its photocatalyst application," vol. 26, pp. 7588-7594, 2015.

[33] P. Li *et al.*, "Design of a ZnMoO 4 porous nanosheet with oxygen vacancies as a better performance electrode material for supercapacitors," vol. 45, no. 20, pp. 9026-9039, 2021.

[34] B. Askri, A. Mhamdi, N. Mahdhi, and M. J. P. B. C. M. Amlouk, "Growth and physical investigations of sprayed ZnMoO4 thin films along with wettability tests," vol. 539, pp. 51-60, 2018.

[35] D. Chernyak *et al.*, "Optical, luminescence and thermal properties of radiopure ZnMoO4 crystals used in scintillating bolometers for double beta decay search," vol. 729, pp. 856-863, 2013.

[36] B.-g. Zhai, Q.-l. Ma, L. Yang, and Y. M. J. M. L. Huang, "Growth of ZnMoO4 nanowires via vapor deposition in air," vol. 188, pp. 119-122, 2017.

[37] R. P. Jia, C. Zhang, and J. Y. J. A. M. R. Xu, "Morphology-controllable synthesis and characterization of ZnMoO4 nanoparticles," vol. 624, pp. 51-54, 2013.

[38] G. Zhang, S. Yu, Y. Yang, W. Jiang, S. Zhang, and B. J. J. o. c. g. Huang, "Synthesis, morphology and phase transition of the zinc molybdates ZnMoO4· 0.8 H2O/α-ZnMoO4/ZnMoO4 by hydrothermal method," vol. 312, no. 11, pp. 1866-1874, 2010.

[39] P. Yadav, E. J. J. o. A. Sinha, and Compounds, "Structural, photophysical and microwave dielectric properties of α-ZnMoO4 phosphor," vol. 795, pp. 446-452, 2019.
[40] S. K. Tiwari *et al.*, "Structural and dielectric properties of Cu-doped α-ZnMoO4 ceramic system for enhanced green light emission and potential microwave applications," vol. 32, no. 10, pp. 12881-12889, 2021.
[41] Y.-R. Jiang, W. W. Lee, K.-T. Chen, M.-C. Wang, K.-H. Chang, and C.-C. J. J. o. t. T. I. o. C. E. Chen, "Hydrothermal synthesis of β-ZnMoO4 crystals and their photocatalytic degradation of Victoria Blue R and phenol," vol. 45, no. 1, pp. 207-218, 2014.
[42] R. Roshani and A. J. M. T. C. Tadjarodi, "Synthesis of ZnMoO4 nanofibers by ultrasonic bath method and investigation of their supercapacitive properties," vol. 26, p. 101794, 2021.
[43] Y. Keereeta, T. Thongtem, and S. J. M. L. Thongtem, "Characterization of ZnMoO4 nanofibers synthesized by electrospinning–calcination combinations," vol. 68, pp. 265-268, 2012.
[44] L. Ivleva, I. Voronina, L. Y. Berezovskaya, P. Lykov, V. Osiko, and L. J. C. R. Iskhakova, "Growth and properties of ZnMoO 4 single crystals," vol. 53, pp. 1087-1090, 2008.
[45] B. Bakiz, F. Guinneton, and J. J. J. M. E. S. Gavarri, "Structural and temperature-dependent vibrational analyses of the non-centrosymmetric ZnMoO4 molybdate," vol. 7, no. 9, pp. 3076-3083, 2016.
[46] Q. Ma, X. Li, G. Li, and Z. J. J. o. M. S. Shao, "Synthesis and electrochemical properties of cubic-like ZnMoO 4 anode materials," vol. 55, pp. 13905-13915, 2020.
[47] B. J. Reddy, P. Vickraman, and A. S. J. B. o. M. S. Justin, "A facile synthesis of novel α-ZnMoO 4 microspheres as electrode material for supercapacitor applications," vol. 42, no. 2, p. 52, 2019.
[48] Z. Shahri, M. Bazarganipour, M. J. S. Salavati-Niasari, and Microstructures, "Controllable synthesis of novel zinc molybdate rod-like nanostructures via simple surfactant-free precipitation route," vol. 63, pp. 258-266, 2013.
[49] J. Ahmed, M. M. Khan, and S. M. J. M. L. Alshehri, "Zinc molybdenum oxide sub-micron plates as electro-catalysts for hydrogen evolution reactions in acidic medium," vol. 284, p. 128996, 2021.
[50] S. Bhattacharya, T. Kar, A. K. Bar, D. Roy, M. Graca, and M. J. S. o. A. M. Valente, "Structural behaviors and optical properties of semiconducting zinc-molybdate glass nanocomposites," vol. 3, no. 2, pp. 284-288, 2011.
[51] Y. Keereeta, T. Thongtem, S. J. S. Thongtem, and Microstructures, "Effect of medium solvent ratios on morphologies and optical properties of α-ZnMoO4, β-ZnMoO4 and ZnMoO4· 0.8 H2O crystals synthesized by microwave-hydrothermal/solvothermal method," vol. 69, pp. 253-264, 2014.
[52] J. Šubčík, L. Koudelka, P. Mošner, L. Montagne, B. Revel, and I. J. J. o. n.-c. s. Gregora, "Structure and properties of MoO3-containing zinc borophosphate glasses," vol. 355, no. 16-17, pp. 970-975, 2009.
[53] T. Basiev, A. Sobol, Y. K. Voronko, and P. J. O. M. Zverev, "Spontaneous Raman spectroscopy of tungstate and molybdate crystals for Raman lasers," vol. 15, no. 3, pp. 205-216, 2000.
[54] S. Li *et al.*, "Near-Zero Thermal Expansion and Phase Transitions in HfMg1− x Zn x Mo3O12," vol. 6, p. 115, 2018.
[55] P. J. Mafa, B. Ntsendwana, B. B. Mamba, and A. T. J. T. J. o. P. C. C. Kuvarega, "Visible light driven ZnMoO4/BiFeWO6/rGO Z-scheme photocatalyst for the degradation of anthraquinonic dye," vol. 123, no. 33, pp. 20605-20616, 2019.
[56] S.-H. Lee, M. J. Seong, C. E. Tracy, A. Mascarenhas, J. R. Pitts, and S. K. J. S. S. I. Deb, "Raman spectroscopic studies of electrochromic a-MoO3 thin films," vol. 147, no. 1-2, pp. 129-133, 2002.